

## MIT Open Access Articles

*Full-waveform based complete moment tensor inversion  
and source parameter estimation from downhole  
microseismic data for hydrofracture monitoring*

The MIT Faculty has made this article openly available. **Please share**  
how this access benefits you. Your story matters.

**Citation:** Song, Fuxian, and M. Nafi Tokso#z. "Full-waveform Based Complete Moment Tensor Inversion and Source Parameter Estimation from Downhole Microseismic Data for Hydrofracture Monitoring." Geophysics 76.6 (2011): WC103. ©2011 Society of Exploration Geophysicists

**As Published:** <http://dx.doi.org/10.1190/geo2011-0027.1>

**Publisher:** Society of Exploration Geophysicists

**Persistent URL:** <http://hdl.handle.net/1721.1/73561>

**Version:** Final published version: final published article, as it appeared in a journal, conference proceedings, or other formally published context

**Terms of Use:** Article is made available in accordance with the publisher's policy and may be subject to US copyright law. Please refer to the publisher's site for terms of use.



## Full-waveform based complete moment tensor inversion and source parameter estimation from downhole microseismic data for hydrofracture monitoring

Fuxian Song<sup>1</sup> and M. Nafi Toksöz<sup>1</sup>

### ABSTRACT

Downhole microseismic monitoring is a valuable tool in understanding the efficacy of hydraulic fracturing. Inverting for the moment tensor has gained increasing popularity in recent years as a way to understand the fracturing process. Previous studies utilize only part of the information in the waveforms, such as direct P- and S-wave amplitudes, and make far-field assumptions to determine the source mechanisms. The method is hindered in downhole monitoring, when only limited azimuthal coverage is available. In this study, we develop an approach to invert for complete moment tensor using full-waveform data recorded at a vertical borehole. We use the discrete wavenumber integration method to calculate full wavefields in the layered medium. By using synthetic data, we find that, at the near-field range, a stable, complete moment tensor can be retrieved by matching the waveforms without additional constraints. At the far-field range, we dis-

cover that the off-plane moment tensor component is poorly constrained by waveforms recorded at one well. Therefore, additional constraints must be introduced to retrieve the complete moment tensor. We study the inversion with three different types of constraints. For each constraint, we investigate the influence of velocity model errors, event mislocations, and data noise on the extracted source parameters by a Monte Carlo study. We test our method using a single well microseismic data set obtained during the hydraulic fracturing of the Bonner sands in East Texas. By imposing constraints on the fracture strike and dip range, we are able to retrieve the complete moment tensor for events in the far-field. Field results suggest that most events have a dominant double-couple component. The results also indicate the existence of a volumetric component in the moment tensor. The derived fracture plane orientation generally agrees with that derived from the multiple event location.

### INTRODUCTION

Downhole microseismic monitoring is a valuable tool for hydrofracture mapping. The locations of microseismic events, with sufficient resolution, provide information on fracture geometry and properties (Warpinski et al., 1998; Phillips et al., 2002). In addition to location, the seismic moment tensor is derived to understand the microseismic source mechanisms and stress state (Nolen-Hoeksema and Ruff, 2001; Baig and Urbancic, 2010). The complete moment tensor of the general source mechanism consists of six independent elements (Aki and Richards, 2002). Some researchers (Phillips

et al., 1998; Warpinski, 1997) observed high S/P-wave amplitude ratios which “could not be explained by tensile opening” (Pearson, 1981) and concluded that the induced events are shear failure along preexisting joints in rocks that surround hydraulic fractures and are caused by elevated pore pressure. Thus, most studies have focused on double-couple mechanisms (Rutledge and Phillips, 2003). However, recent studies have shown the existence of nondouble-couple mechanisms for some hydrofracture events (Šílený et al., 2009; Warpinski and Du, 2010). The knowledge of nondouble-couple components, especially the volumetric component, is essential to understand the fracturing process. Moreover, Vavryčuk (2007)

Manuscript received by the Editor 31 January 2011; revised manuscript received 31 July 2011; published online 27 December 2011; corrected version published online 18 January 2012.

<sup>1</sup>Massachusetts Institute of Technology, Department of Earth, Atmospheric and Planetary Sciences, Earth Resources Laboratory, Cambridge, Massachusetts, USA. E-mail: fxsong@mit.edu; toksoz@mit.edu.

© 2011 Society of Exploration Geophysicists. All rights reserved.

showed that, for shear faulting on nonplanar faults, or for tensile faulting, the deviatoric source assumption is no longer valid and can severely distort the retrieved moment tensor and bias the fault-plane solution. Therefore, the complete moment tensor inversion is crucial not only to the retrieval of the volumetric component but also to the correct estimation of the fault-plane solution.

Currently, most moment tensor inversion methods rely only on far-field direct P- and S-wave amplitudes (Nolen-Hoeksema and Ruff, 2001; Vavryčuk, 2007; Jechumtálová and Eisner, 2008; Wapinski and Du, 2010). Vavryčuk (2007) used the far-field approximation of the P- and S-wave Green's function in homogeneous isotropic and anisotropic media to show that a single-azimuth data set recorded in one vertical well cannot resolve the dipole perpendicular to the plane of geophones and the hypocenter. Thus, the complete moment tensor of the general source mechanism is underdetermined with data from one-well. To overcome this problem, previous studies have proposed using data recorded in multiple monitoring wells at different azimuths (Vavryčuk, 2007; Baig and Urbancic, 2010). Unfortunately, downhole microseismic monitoring data sets are frequently limited to a single array of geophones in one vertical well. Therefore, the issue of complete moment tensor inversion from one-well data remains unsolved.

In this paper, we try to address this problem from the standpoint of full-waveform inversion. We propose a full-waveform approach for moment tensor inversion using data from one monitoring well. It uses the discrete wavenumber integration method to calculate elastic wavefields in the layered medium. By matching the waveforms across the geophone array, we show that, when the events are close to the monitoring well, the inversion can be stabilized so that the complete moment tensor can be retrieved from data recorded in a single borehole without making additional source assumptions. We quantify the closeness of events by studying the condition number of the sensitivity matrix. For events far from the monitoring well, we demonstrate that additional constraints must be introduced to retrieve the off-plane dipole component (also pointed out by Vavryčuk [2007] and Jechumtálová and Eisner [2008]). Three types of constraints have been studied in this paper to invert the complete moment tensor for events at far-field. Furthermore, we investigate the influence of velocity model errors, source mislocations, and data noise on the extracted source parameters using synthetic data. Finally, we describe the application of the constrained inversion to a field data set from East Texas. By applying the constraint on the fracture strike and dip range, we show that a reliable, complete moment tensor solution and source parameters can be obtained for each event.

## METHODOLOGY

### Full-waveform based complete moment tensor inversion

The complete moment tensor of a microseismic event is characterized by the six independent elements of the 3 by 3 symmetric moment tensor matrix  $m_{jk}$ . To improve the complete moment tensor inversion with a single borehole, we use all phases that are embedded in the full-waveform data. Our approach starts from fast, full elastic waveform modeling in a layered medium with the discrete wavenumber integration method (DWN; Bouchon, 2003). The  $i$ th component (north, east, down) of the observed waveform at geophone  $n$  is modeled as

$$v_i(x_r^n, x_s, t) = \sum_{j=1}^3 \sum_{k=1}^3 m_{jk} G_{ij,k}(x_r^n, x_s, t) * s(t), \quad (1)$$

where  $*$  denotes the convolution operation (same hereinafter);  $G_{ij,k}(x_r^n, x_s, t)$ , the spatial derivative of the Green's function, is the  $i$ th component of the elementary seismograms at the  $n$ th geophone  $x_r^n$  due to a point moment tensor source  $m_{jk}$  at  $x_s$ ;  $s(t)$  is the source time function. In this study, a smooth ramp function with a center frequency of 550 Hz is used as  $s(t)$ , according to the spectral analysis of field data. The sampling frequency is 4 kHz in both synthetic and field study. Considering that the moment tensor matrix  $m_{jk}$  has only six independent elements, equation 1 can be written as

$$\sum_{l=1}^6 A_{il}(x_r^n, x_s, t) M_l(x_s) = v_i(x_r^n, x_s, t), \quad (2)$$

where  $M_l$  is the  $l$ th moment tensor element:  $M_1 = m_{11}$ ,  $M_2 = m_{22}$ ,  $M_3 = m_{33}$ ,  $M_4 = m_{12}$ ,  $M_5 = m_{13}$ ,  $M_6 = m_{23}$ , while  $A_{il}$  denotes the  $i$ th component of the elementary seismograms at geophone  $x_r^n$  due to a point moment tensor source  $M_l$  at  $x_s$ . In matrix form, equation 2 becomes

$$\mathbf{A}\mathbf{M} = \mathbf{D}. \quad (3)$$

Here the sensitivity matrix  $\mathbf{A}$  (i.e., data kernel) is composed of six columns, with each column consisting of the elementary seismograms from a point moment tensor source  $M_l$ . The six element vector  $\mathbf{M}$  represents the complete moment tensor:

$$\mathbf{M} = [M_1, M_2, M_3, M_4, M_5, M_6]^T. \quad (4)$$

Data column vector  $\mathbf{D}$  is comprised of all available components recorded at all geophones ranging from time  $t_{0n}$  to  $(t_{0n} + T_n)$ , where  $t_{0n}$  and  $T_n$  are the starting time and the duration of recorded data used in the inversion from geophone  $n$ , respectively. In this study, we choose  $T_n$  to include both P- and S-wave trains and keep it fixed for all  $N$  geophones. The starting time  $t_{0n}$  is determined from the event origin time  $t_0$  and the P-wave traveltimes from the event to geophone  $n$ . Event origin time is obtained by a grid search around its initial estimate within the dominant signal period. The initial estimate of the origin time can be found by cross-correlating the synthetic and observed waveforms.

To reduce the influence from errors in source locations, during the inversion, we also perform a grid search around the initial location. The spatial search range and grid size are selected based on the location uncertainty. The uncertainty in locations from a vertical array is estimated from the standard deviations of P- and S-wave arrival times and P-wave polarization angles (Eisner et al., 2010). For the field data, we calculate standard deviations and obtain 3.0 m (10 ft) in the radial direction, 7.6 m (25 ft) in the vertical direction, and 5° in P-wave derived back-azimuths. We further determine the location uncertainty in the horizontal directions (north, east) from the standard deviations of the radial distances and P-wave derived back-azimuths for a monitoring array at a typical distance of 100.6 m (330 ft). The standard deviation is estimated to be 9.1 m (30 ft). Therefore, in this study, we use a spatial grid of 5 ft and a spatial search cube with measurements of 15 × 15 × 11 grids (north, east, down). The best solution of the event location

$x_s$ , origin time  $t_0$ , and moment tensor  $M_I$  is determined by minimizing the squared L-2 norm of the waveform fitting error:

$$J(x_s, t_0, M_I) = \sum_{n=1}^N \sum_{i=1}^{N_c} \sum_{k=1}^{N_t} (d_i(x_r^n, x_s, k\Delta t) - v_i(x_r^n, x_s, k\Delta t))^2, \quad (5)$$

where  $N$  is the number of geophones,  $N_t$  is the number of time points, and  $N_c$  is the number of components used in the inversion. The sampling interval of the recorded data is  $\Delta t$ .

To further stabilize the inversion, both synthetic data and observed data are band-pass filtered. Based on the spectral analysis of the signal and pre-event noise from the field data example, a band-pass filter of [200, 900] Hz is used in this paper. For  $N$  geophones, the sensitivity matrix  $\mathbf{A}$  has a size of  $NN_cN_t$  by 6. In this study, as we will explain in the field study, only two horizontal components are used in the inversion due to poor signal-to-noise ratios (S/Ns) in the vertical component. Therefore, in this study  $N_c = 2$ . However, the method itself is not limited to two components. If matrix  $\mathbf{A}$  is well-conditioned, a least-squares solution to the overdetermined system can be obtained using the generalized inverse:

$$\mathbf{M} = (\mathbf{A}^T \mathbf{A})^{-1} \mathbf{A}^T \mathbf{D}. \quad (6)$$

The condition number of matrix  $\mathbf{A}$  will be discussed in the synthetic study.

The processing steps can be summarized as follows:

- 1) generate a Green's function library, calculate the elementary seismograms, and apply the band-pass filter to the elementary seismograms for each possible event location;
- 2) apply the same band-pass filter to the recorded waveforms;
- 3) estimate the initial event origin time at every possible event location;
- 4) carry out a cascaded grid search around the initial estimated event origin time and location. For each event location, conduct a grid search on event origin time. For each origin time and location, find the least-squares solution  $M_I(x_s, t_0)$  according to equation 6, and evaluate the L-2 waveform fitting error according to equation 5;
- 5) determine the best solution of moment tensor, event location, and origin time with the least amount of waveform fitting error.

### Source parameter estimation

The complete moment tensor can be decomposed into the isotropic (ISO), compensated linear vector dipole (CLVD), and double-couple (DC) components. In this paper, we use the decomposition of a moment tensor proposed by Vavryčuk (2001). The symmetric moment tensor matrix  $m_{jk}$  can be diagonalized and represented as the sum of the deviatoric moment  $M^{\text{dev}}$  (i.e., the moment tensor with zero volumetric component), and the isotropic moment  $M^{\text{iso}}$ . Parameter  $\varepsilon$  is introduced to measure the size of CLVD relative to DC:

$$\varepsilon = -\frac{\lambda_{\min}^{\text{dev}}}{|\lambda_{\max}^{\text{dev}}|}, \quad (7)$$

where  $\lambda_{\min}^{\text{dev}}$  and  $\lambda_{\max}^{\text{dev}}$  are the minimum and maximum absolute eigenvalues of the deviatoric moment, respectively. For a pure

DC  $\varepsilon = 0$ , and for a pure CLVD  $\varepsilon = \pm 0.5$ . Parameter  $\varepsilon$  is positive for tensile sources and negative for compressive sources. The percentages of each component (ISO, CLVD, DC) can be calculated as

$$c^{\text{ISO}} = \frac{1}{3} \frac{\text{trace}(m_{jk})}{M_0}, \quad (8)$$

$$c^{\text{CLVD}} = 2\varepsilon(1 - |c^{\text{ISO}}|), \quad (9)$$

$$c^{\text{DC}} = 1 - |c^{\text{ISO}}| - |c^{\text{CLVD}}|, \quad (10)$$

where  $M_0$  is the seismic moment in  $\text{N} \cdot \text{m}$ , defined as the largest absolute eigenvalue of the moment tensor matrix  $m_{jk}$

$$M_0 = \max_{\{i\}} |\lambda_i|. \quad (11)$$

The moment magnitude is calculated as

$$M_w = \frac{2}{3} \log_{10}(M_0) - 6.607. \quad (12)$$

According to Jost and Hermann (1989), the eigenvector  $\mathbf{b}$  of the moment tensor matrix  $m_{jk}$  corresponding to the intermediate eigenvalue gives the null axis, while the eigenvectors  $\mathbf{t}$  and  $\mathbf{p}$  corresponding to the maximum and minimum eigenvalue give the tension and compression axis, respectively. The fracture plane normal  $\mathbf{v}$  and the slip vector  $\mathbf{u}$  can be derived from the  $\mathbf{t}$  and  $\mathbf{p}$  axes as

$$\mathbf{u} = \frac{1}{\sqrt{2}}(\mathbf{t} + \mathbf{p}), \quad \mathbf{v} = \frac{1}{\sqrt{2}}(\mathbf{t} - \mathbf{p}). \quad (13)$$

The fracture plane solutions, including strike  $\phi$ , dip  $\delta$ , and rake  $\lambda$ , can be further derived from the fracture plane normal  $\mathbf{v}$  and the slip vector  $\mathbf{u}$  (Jost and Hermann, 1989).

## SYNTHETIC STUDY

### Condition number of the sensitivity matrix in full-waveform inversion

In this section, we study the influence of borehole azimuthal coverage and the source-receiver distance on the condition number of the sensitivity matrix and discuss its implications in complete moment tensor inversion using synthetic data from a single well.

Figure 1 gives the source-receiver configuration. In this experiment, we fix the microseismic event at (0, 0, 3946 m). An array of six-level three-component (3C) geophones is deployed in each vertical well at the same depth range as the field setup from 3912 m (12,835 ft) to 3944 m (12,940 ft). The horizontal location of the well is adjusted so that the mean source-receiver distance falls into the range between  $4\lambda_s$  and  $36\lambda_s$ , where  $\lambda_s$  is the dominant S-wave wavelength. For each mean source-receiver distance, we calculate the elementary seismograms and apply the [200, 900] Hz band-pass filter to obtain the filtered elementary seismograms and form the sensitivity matrix  $\mathbf{A}$ . Figure 2 shows the one-dimensional (1D) P- and S-wave velocity models derived from the field study. We use this velocity model to generate elementary seismograms for the condition number study.

Figure 3a shows the condition number of the sensitivity matrix  $\mathbf{A}$  as a function of both borehole azimuthal coverage and the mean source-receiver distance when all 3C data are used in the inversion. Three observations are clearly seen on Figure 3a. First, the condition number increases dramatically with the increased mean source-receiver distance for the one-well case. This signifies that the resolvability of complete moment tensors deteriorates at far-field when only one-well data are used in moment tensor inversion. In addition,

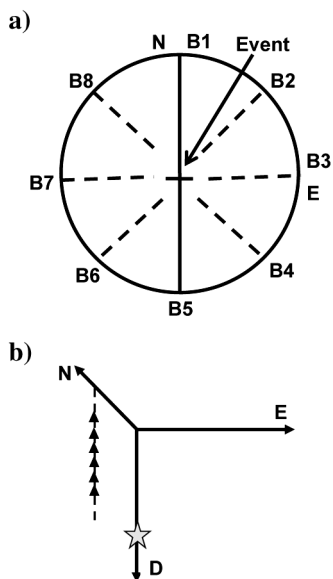


Figure 1. (a) Horizontal plane view of the source and receiver array distribution in the condition number study. The microseismic event, labeled as the plus sign, lies in the center, with eight monitoring wells, B1 to B8, evenly spreading from the north direction to the north-west direction. The azimuthal separation between two adjacent wells is  $45^\circ$ . (b) 3D view of the single well configuration used in the inversion study (B1 well, at the azimuth of  $N0^\circ E$ ). The gray star denotes the hypocenter location of the microseismic event, while the six receivers, deployed in the well, are shown as black triangles. (North: x, East: y, and Down: z)

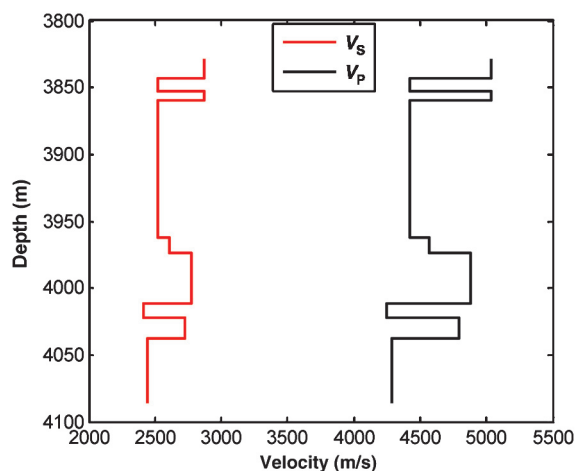


Figure 2. One-dimensional P- and S-wave velocity model derived from field study.

the eigenvector corresponding to the minimum eigenvalue gives the least resolvable moment tensor element. In the case of well B1 at the azimuth of  $0^\circ$ , the off-plane element  $m_{22}(m_{ee})$  is the least resolvable moment tensor element. This is consistent with the far-field study in the homogeneous media. Second, the condition number for the multiple-well cases is significantly lower than that of the one-well case at large source-receiver distances, while the condition number is low for all cases at small source-receiver distances. This indicates that complete moment tensor inversion is possible, even with one-well data, when the receivers are at the near-field range. There is no clear distinction between near-field and far-field. At a noise level of

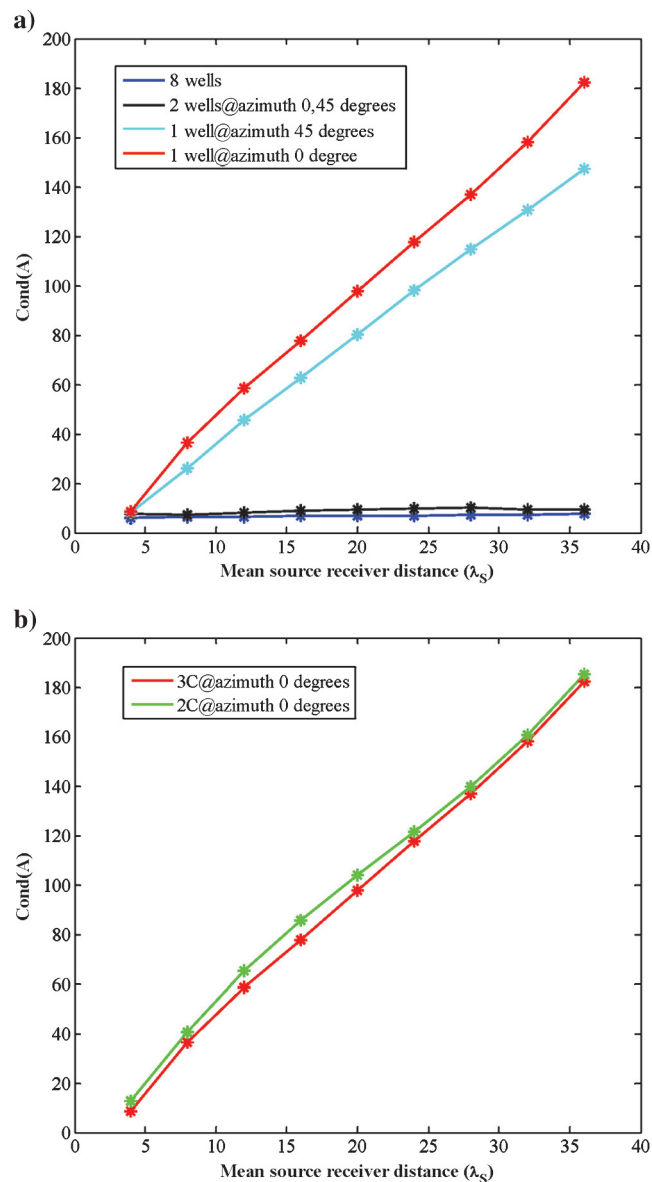


Figure 3. The condition number of the waveform sensitivity matrix  $\mathbf{A}$ , plotted as a function of the mean source-receiver distance, shown in multiples of the dominant S-wave wavelength. The matrix  $\mathbf{A}$  is formed using: (a) three-component full-waveforms under different well configurations; (b) full-waveforms of three components or two horizontal components from the six-receiver array in the B1 well at the azimuth of  $0^\circ$ . Well azimuth is defined as east of north.



10%, as is the case in the following synthetic study, a rule of thumb is that at a mean source-receiver distance that is less than five times the S-wave wavelength, a stable complete moment tensor solution can be determined from the one-well data. Finally, the condition number of the two-well case is similar to that of the eight-well case. This seems to imply that, with two wells separated at  $45^\circ$ , the resolvability of complete moment tensor is comparable to that of eight wells, although, for a more complex scenario, such as a laterally heterogeneous medium, eight wells can bring additional benefits in enhancing the source azimuthal coverage and improving S/Ns of recorded events. The condition number of the two-well case barely increases with increased source-receiver distances. This indicates that the complete moment tensor inversion is feasible for both near-field and far-field with two-well data. Figure 3b compares the condition number of the sensitivity matrix of the one-well case using all 3Cs and only two horizontal components. The result suggests that two horizontal components have a similar capability of constraining the moment tensor as three components.

### Complete moment tensor inversion of events in the near-field

As we see in the previous section, for events that are close to the monitoring well, it is possible to invert the complete moment tensor from one-well data. Figure 4a shows the total wavefields of the two horizontal components recorded in the well B1 at an azimuth of  $0^\circ$ . The synthetic data are generated with the reference velocity model plotted in Figure 2. Without losing generality, a nondouble-couple microseismic source with 74% of DC, 15% of CLVD, and 11% of ISO component is used in the simulation. The microseismic source has a strike of  $108^\circ$ , a dip of  $80^\circ$ , and a rake of  $43^\circ$ . The distance from the source to six receivers ranges from one to six dominant S-wave wavelengths. At a distance of one to two dominant S-wave wavelengths, complex waveforms are seen on geophones 5 and 6, due to the near-field effects. At a distance larger than three S-wave wavelengths, distinct P and S phases are observed on geophones 1 to 4. Figure 4b gives the near-field terms of the two horizontal components. It is seen on Figure 4b that the near-field terms decrease quickly as the source-geophone distance increases. To quantify the contribution of near-field information, we calculate the peak amplitude ratio of the near-field term to the total wavefields for each component on each geophone. The average peak amplitude ratios of the two horizontal components are 9%, 11%, 14%, 18%, 22%, and 60% for geophones 1 to 6, respectively. Therefore, the major contribution of near-field information to the inversion comes from geophones 5 and 6, which are close to the microseismic source.

Figure 5a shows the noisy seismograms by adding zero-mean Gaussian noise with a standard deviation reaching 10% of the average absolute maximum amplitude of the two components across all six geophones. Figure 5b gives the band-pass filtered data used to invert for the complete moment tensor.

The P- and S-wave velocity models are randomly perturbed up to half of the velocity difference between adjacent layers so that the sign of the velocity difference between adjacent layers does not change. The perturbation is independent between different layers and P- and S-wave velocities are independently perturbed. The perturbed velocity model is used as the approximate velocity model for moment tensor inversion throughout the paper. As mentioned in the methodology section, to mimic the field example, the event location is randomly perturbed up to 9.1 m (30 ft) in the north and east

directions and 7.6 m (25 ft) in the vertical direction. In the inversion, a grid search is carried out around the randomly perturbed event location. The moment tensor solution corresponding to the minimum L-2 waveform fitting error is selected as the inversion result. Figure 6 gives the best waveform fitting for one Gaussian noise realization. A good agreement between modeled data in black and band-pass filtered synthetic data in red is seen on both components.

The source parameters are then estimated from the inverted complete moment tensor. To obtain statistically relevant results, we perform 100 moment tensor inversions and source parameter estimations, each with a different noise realization. Figure 7 shows

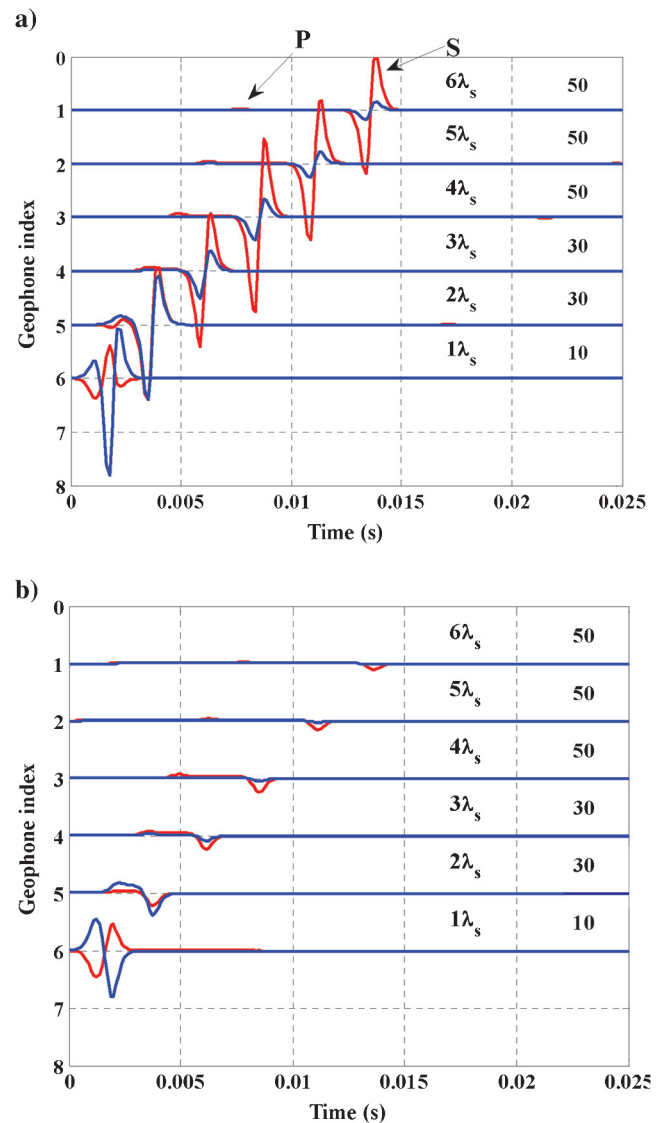


Figure 4. Synthetic seismograms recorded by the six receivers in well B1 from a nondouble-couple microseismic source (horizontal components only, with the north component in red and the east component in blue). (a) Total wavefields. (b) Near-field terms only. Each source-receiver distance is shown as multiples of the dominant S-wave wavelength ( $\lambda_s = 5.2$  m). The average source-receiver distance is 18.3 m (60 ft). The scaling factor for each trace is also listed. The source has a strike of  $108^\circ$ , a dip of  $80^\circ$ , and a rake of  $43^\circ$ . The source is composed of 74% DC component, 15% CLVD component, and 11% isotropic component.

the histograms of the ISO, CLVD, DC, seismic moment, strike, dip, rake errors for the nondouble-couple event. The average absolute errors in the percentages of the ISO, CLVD, and DC components are about 4%, 4%, and 6%, respectively, while the average absolute relative error in seismic moment is around 6%. The average absolute error in the strike, dip, and rake is less than  $2^\circ$ . Moreover, the complete moment tensor inversion, using the horizontal component data from geophones 5 and 6, gives comparable results in the inverted source parameters. This indicates that the near-field information contributed to the retrieval of  $m_{22}(m_{ee})$  mainly comes from geophones 5 and 6. Considering the inaccuracies in the source location and velocity model together with 10% Gaussian noise, the inverted source parameters agree well with the true values. This demonstrates that for events in the near-field (i.e., at a mean source-receiver distance less than five times the S-wave wavelength), the complete moment tensor inversion is feasible with one-well data using only two horizontal components. The retrieval of  $m_{22}$  with one-well data at near-field is further illustrated in Appendix A.

### Complete moment tensor inversion of events in the far-field

As we see in the condition number study, for events that are far from the monitoring well (i.e., at a mean source-receiver distance greater than five times the S-wave wavelength), the condition

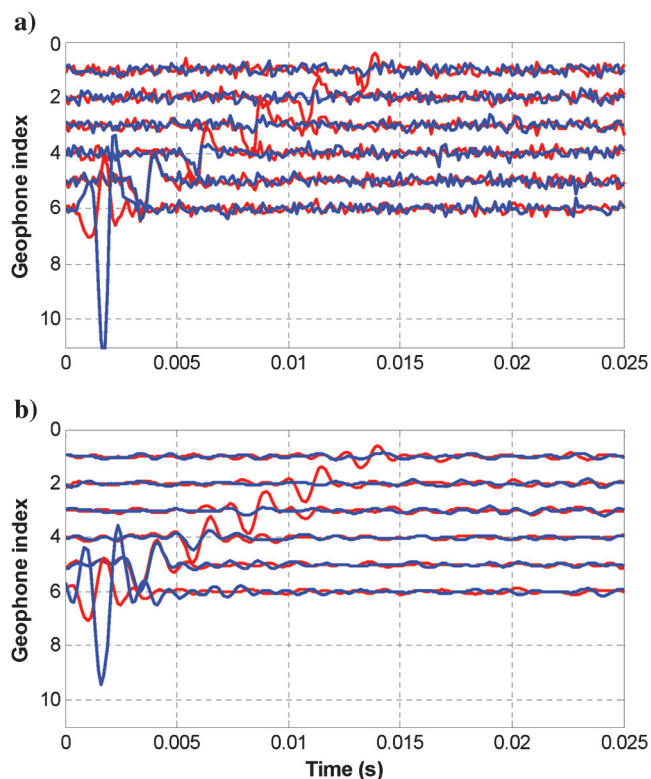


Figure 5. Synthetic data from the nondouble-couple microseismic source. (a) After adding 10% Gaussian noise to the horizontal component data shown in Figure 4. (b) After applying the [200, 900] Hz band-pass filter to the noise contaminated data in (a). The north component is plotted in red, while the east component is shown in blue. The scaling factor is 30.

number of the sensitivity matrix using one-well data is high compared to that of near-field events. In the case of well B1 at the azimuth of  $0^\circ$ , the off-plane element  $m_{22}$  is the least resolvable moment tensor element from full-waveform inversion.

Figure 8 shows the condition number of the sensitivity matrix when inverting for all six moment tensor elements and five moment tensor elements, except  $m_{22}$ , with only two horizontal components. It is observed that at far-field in the layered medium, when  $m_{22}$  is excluded from the inversion, the condition number of the sensitivity matrix is reduced to the level of complete moment tensor inversion at near-field. This shows that the full waveforms are mainly sensitive to the five moment tensor elements, except  $m_{22}$ . Therefore, for events in the far-field, additional constraints must be introduced to retrieve  $m_{22}$ .

The basic idea of the constrained inversion is to invert for the rest of the five moment tensor elements using waveforms, assuming a known value of  $m_{22}$ . The source parameters are then estimated from the complete moment tensor as a function of  $m_{22}$ . As suggested by Jechumtálová and Eisner (2008), we test the  $m_{22}$  value between  $-10M_5$  and  $10M_5$ , where  $M_5$  is the maximum absolute value of the five inverted elements. By using a priori source information (for example, fracture orientations) as constraints  $m_{22}$  can be determined. Finally, the complete moment tensor and the source parameters are derived.

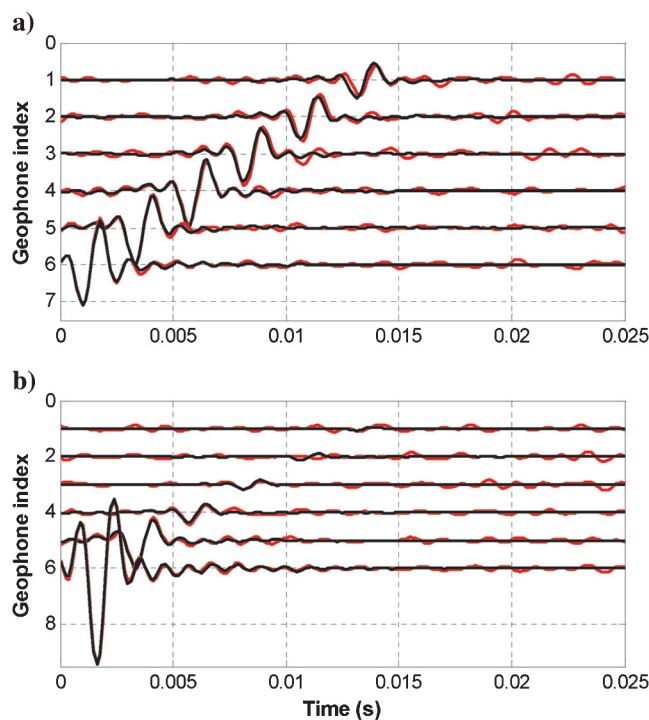


Figure 6. Comparison between the modeled data in black and the band-pass filtered synthetic data in red for the nondouble-couple source in Figure 4. The modeled data are generated from the inverted microseismic moment tensor matrix (six independent elements). The unconstrained inversion is performed with the band-pass filtered horizontal components in Figure 5b). (a) North component plot. (b) East component plot. The scaling factor is 30. All the inversions in this study are performed with only horizontal components from well B1 and use the approximate velocity model and the mislocated source (see text).

It is also seen from Figure 8 that in the layered medium, the condition number is not a monotonous function of mean source-receiver distance for the case of constrained inversion, while the condition number in the homogeneous medium is a monotonous function of mean source-receiver distance. This can be explained by the difference in the take-off angle coverage at the source between the homogeneous medium and the layered medium.

Eaton (2009) pointed out that in the homogeneous medium the condition number is inversely proportional to the solid angle at the source subtended by the geophone array. In the homogeneous medium only direct rays are available, and, therefore, the take-off angle coverage at the source is fully characterized by the solid angle. However, in the layered medium, as is the case in this study, not

only direct but also reflected and refracted rays exist, even if the source and geophone array are situated in the same layer. Therefore, the take-off angle coverage at the source has been increased in the layered medium than in the homogeneous medium scenario, considering the additional reflected and refracted rays.

The increase in the take-off angle coverage at the source produces a decreased condition number. Hence, in the layered medium, the condition number is controlled by the geometry of the receiver array relative to not only the source but also the velocity model. An increase in the mean source-receiver distance will reduce the take-off angle coverage of the direct rays. It may, however, increase the take-off angle coverage from reflected and refracted rays. There is also a critical distance for the refracted rays to occur. Thus, the nonmonotonous behavior for the constrained inversion case in the layered medium is probably due to the complex interaction of the increased take-off angle coverage from the reflected and refracted rays and the decreased take-off angle coverage of direct rays.

Several types of constraints may be applied in the constrained inversion. In this paper, we study three types of constraints. In type I constraint, the range of the strike and dip is assumed to be known. This will give a permissible range of  $m_{22}$  values. We further assume that the source mechanism is mostly double-couple, and therefore

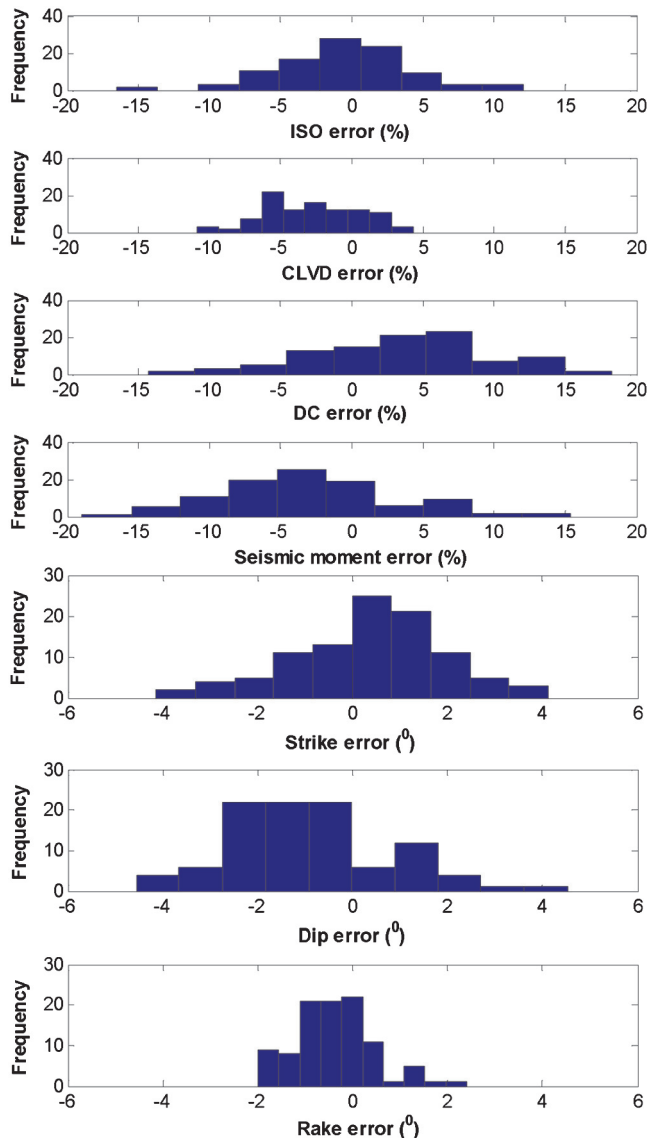


Figure 7. The histograms of errors in the inverted source parameters. The microseismic source is nondouble-couple. The true moment tensor and source-receiver locations are described in Figure 4. The unconstrained inversion is performed with the band-pass filtered horizontal components from well B1.

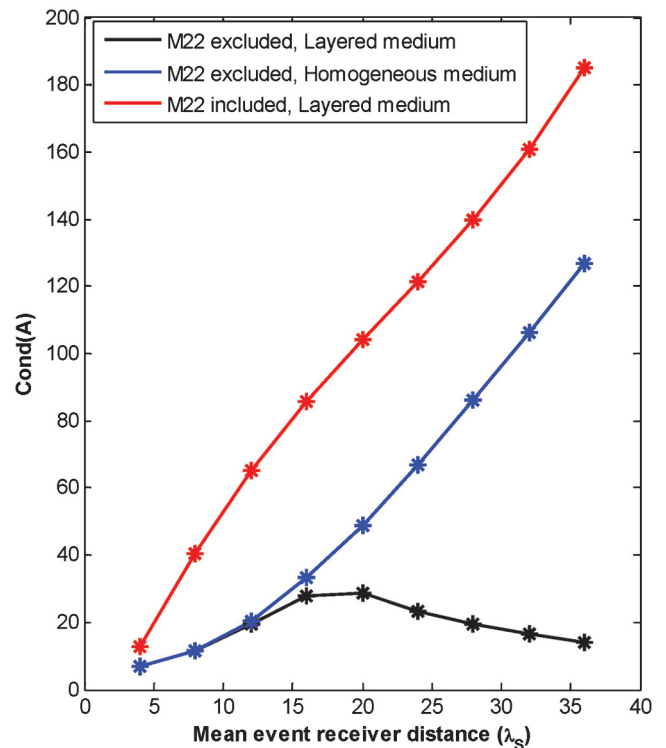


Figure 8. The condition number of the waveform sensitivity matrix  $\mathbf{A}$ , plotted as a function of the mean source-receiver distance, shown in multiples of the dominant S-wave wavelength. The matrix  $\mathbf{A}$  is formed using full waveforms of two horizontal components recorded by the six-receiver array in the monitoring well B1. The condition number of the unconstrained inversion in the layered medium for all six independent moment tensor elements is plotted in red, while the condition numbers of the constrained inversion in the layered and homogeneous medium for five independent moment tensor elements, except  $m_{22}$ , are shown in black and blue, respectively.



we determine the  $m_{22}$  value by maximizing the DC percentage within that permissible range. Figure 9 gives an example of applying type I constraint. In this example, we use the same nondouble-couple source and source-receiver configuration as the previous near-field case, shown in Figure 4. The mean source-receiver distance increases to 91.4 m ( $17.5\lambda_s$ ). In Figure 9 we invert for the five moment tensor elements, except  $m_{22}$ , from the band-pass filtered noise-free horizontal component data recorded in well B1. Assuming that the strike and dip range is known to be  $\pm 15^\circ$  around the true values, the cyan strip gives the permissible range of  $m_{22}$  values. The vertical line in green denotes the determined  $m_{22}$  value by maximizing the DC percentage within that permissible range.

In type II constraint, we assume that the exact strike value is known so that the  $m_{22}$  value is determined directly. In type III constraint, the fracture plane solution is unknown; instead, we assume the event is predominantly double-couple. This suggests that the  $m_{22}$  value is obtained by maximizing the DC percentage among all possible values.

Table 1 compares the nondouble-couple source inversion results under three different constraints using noise-free horizontal component data from well B1. For each constraint, it shows the deviation of the inverted source parameters from the original input source parameters. Two observations are seen in Table 1. First, in this case, type I constraint gives the same result as type III constraint; this indicates the strike and dip range from type I constraint may be too large to bring additional information in constraining  $m_{22}$  for this noise-free data set. Second, among all three constraints, type II gives the least error in the inverted source parameters. This is because maximizing the DC percentage, as in type I and III, is not a good assumption about the actual source (the true moment tensor is nondouble-couple, with 74% of the DC, 15% of the CLVD, and 11% of the ISO component). Moreover, knowing the strike value

not only helps constrain the fracture plane geometry of the strike, dip, and rake values, but also enables the recovery of  $m_{22}$  and, eventually, moment component percentages.

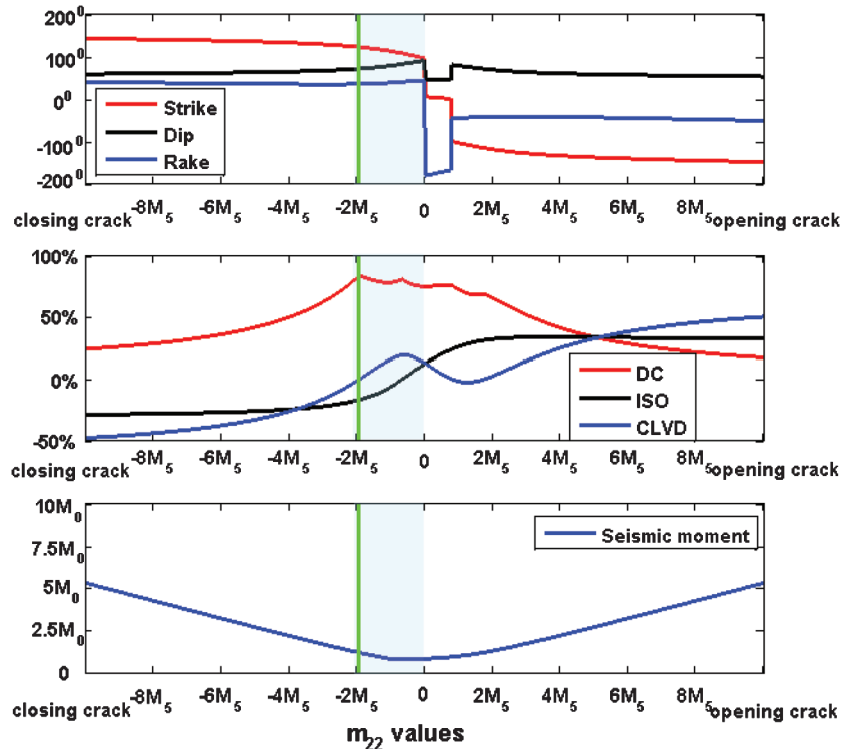
Next, we add 10% Gaussian noise into the synthetic horizontal component data and perform 100 moment tensor inversions on the band-pass filtered noisy data, each with a different noise realization. The histograms of the inverted source parameters are plotted in Figure 10 for this nondouble-couple source.

Table 2 summarizes the statistics of the histograms in Figure 10. It gives the mean absolute errors in the inverted source parameters under three different inversion constraints. With data noise, we observe that mean absolute errors in the strike, dip, and rake of the type I constraint are less than those of the type III constraint; this implies that even a rough knowledge of the strike and dip range helps reduce the uncertainty of  $m_{22}$  and, eventually, the fracture plane solution (strike, dip, and rake). The errors in strike and dip estimates are also bounded, as specified in the type I constraint ( $\pm 15^\circ$  for Table 2).

Knowing the exact strike value, as in the type II constraint, greatly reduces the errors in the estimated fracture plane solution and seismic moment. However, the mean absolute errors in the CLVD, DC percentages seem to be slightly higher than those of the type I constraint. This may indicate a trade-off in errors between the fracture plane solution and the moment component percentages for the noisy data scenario. Furthermore, a comparison between the noise-free case (Table 1) and the 10% Gaussian noise case (Table 2) shows that random noise does not cause a serious distortion in the inverted source parameters; the closeness of the applied constraints to the true source model probably plays a bigger role in the constrained moment tensor inversion for events at far-field.

Similar to Figure 10, we conduct a Monte Carlo study of the constrained moment tensor inversion for a double-couple source

Figure 9. Synthetic test on nondouble-couple source mechanism: Top plot: strike (red line), dip (black line), and rake (blue line) of DC component of the full moment tensor as a function of the unconstrained component  $m_{22}$ . Middle plot: components of the full moment tensor as a function of the unconstrained component  $m_{22}$ . Red line, double-couple (DC); black line, isotropic (ISO); blue line, compensated linear vector dipole (CLVD). Bottom plot: inverted seismic moment as a function of the unconstrained component  $m_{22}$ , with  $M_0$  as the true seismic moment. The inversion is performed with the type I constraint, where the range of the inverted strike and dip is specified a priori. The cyan strip represents the allowed strike and dip range. The constrained inversion recovers  $m_{22}$  by seeking to maximize the DC percentage within the cyan strip. The correct solution is represented by the vertical green line. The inversion is performed with noise-free data from well B1. The average source-receiver distance is 91.4 m (300 ft). The true moment tensor is described in Figure 4.



with the same strike, dip, and rake values as the previous nondouble-couple case. The histograms of the inverted source parameters are given in Figure 11.

Table 3 summarizes the double-couple source inversion results under three different constraints. We see that maximizing DC percentage, as in the type III constraint, gives the smallest mean absolute errors in component percentage estimates, while knowing strike value, as in the type II constraint, helps reduce the errors in the fracture plane solution. In general, from Tables 2 and 3, we see that, with a reasonable amount of data noise and errors in velocity model and source location, the complete moment tensor can be inverted from one-well data at far-field by imposing additional constraints, such as the fracture plane orientation.

It is worth noting that the synthetic study conducted here is not a complete test on the influence of velocity model errors because only one random perturbation of the velocity model is used in the inversion. Furthermore, one should be aware that the influence of velocity model errors can be more serious when the source and the geophone array are situated in two different velocity layers.

## FIELD STUDY

### Field setup

A microseismic survey was conducted during the hydraulic fracturing treatment of the Bonner sands in the Bossier play at a depth from  $\approx 3956$  m (12,980 ft) to  $\approx 3981$  m (13,060 ft). The

**Table 1. Summary of microseismic source inversion with one-well data under different constraints. The inversion is performed with noise-free data and uses the approximate velocity model and the mislocated source. The average source-receiver distance is 91.4 m (300 ft). The true moment tensor of this nondouble-couple source is described in Figure 4.**

Errors in the inverted source parameters	Type of inversion constraints		
	I	II	III
Isotropic component percentage (%)	-28	-12	-28
CLVD component percentage (%)	-15	4	-15
DC component percentage (%)	9	6	9
Seismic moment (%)	24	-16	24
Strike ( $^{\circ}$ )	14	0	14
Dip ( $^{\circ}$ )	-9	1	-9
Rake ( $^{\circ}$ )	-8	-4	-8

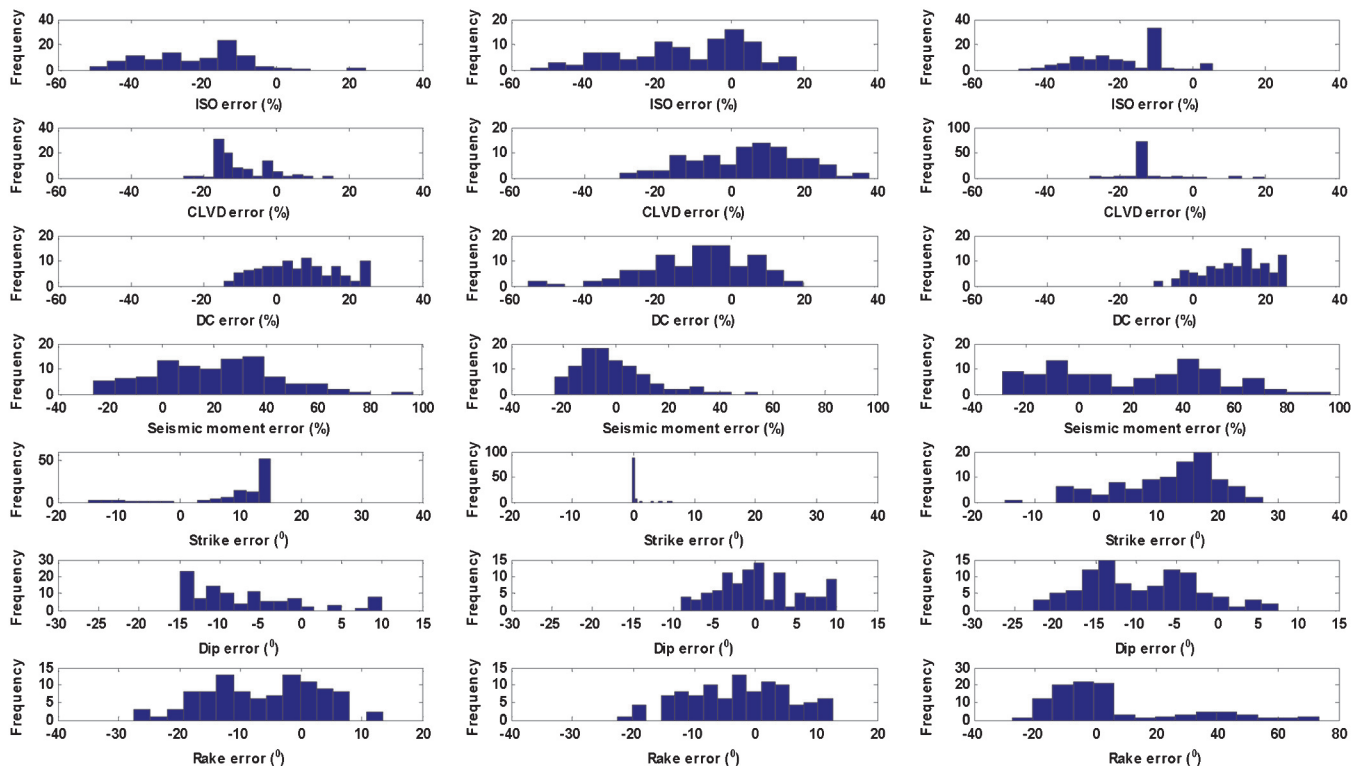


Figure 10. The histograms of errors in the inverted source parameters (nondouble-couple source). The true moment tensor and the source-receiver configuration are described in Figure 9. The constrained inversion is performed with 10% Gaussian noise contaminated data. Left column: inversion with the type I constraint. Middle column: inversion with the type II constraint. Right column: inversion with the type III constraint. See main text for details on different constraint types.

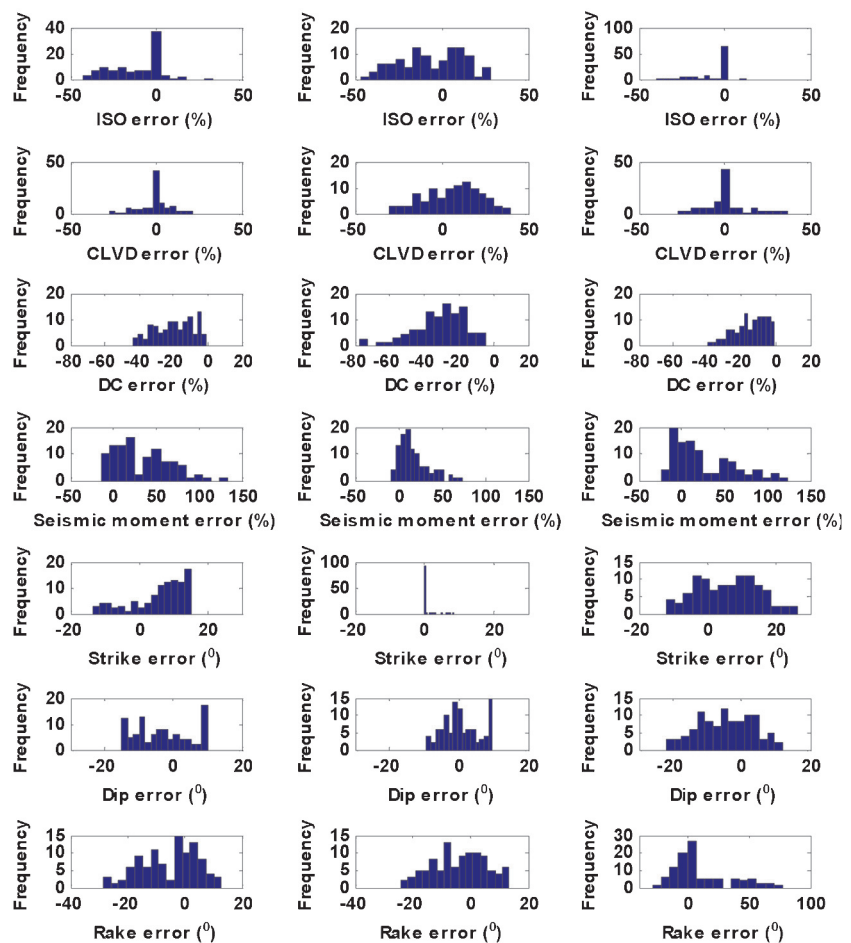
**Table 2. Statistics of nondouble-couple microseismic source inversion with one-well data under different constraints (refer to Figure 10). The inversion is performed with 10% Gaussian noise contaminated data and uses the approximate velocity model and the mislocated source. The average source-receiver distance is 91.4 m (300 ft). The true moment tensor is described in Figure 4.**

Mean absolute errors in the inverted source parameters	Type of inversion constraints		
	I	II	III
Isotropic component percentage (%)	23	16	20
CLVD component percentage (%)	11	13	14
DC component percentage (%)	10	13	13
Seismic moment (%)	25	11	30
Strike (°)	12	0	13
Dip (°)	9	4	10
Rake (°)	9	7	14

microseismic data were collected using a twelve-level, three-component geophone array deployed in the vertical monitoring well at a depth from 3874 m (12,710 ft) to 3944 m (12,940 ft). The treatment well is approximately 151 m (495 ft) away from the monitoring well. The recorded data were analyzed and located for hydraulic fracturing mapping as outlined by Griffin et al. (2003) and Sharma et al. (2004). The velocity model for location, shown in Figure 2, was derived from the well logging data and calibrated using perforation shots (Warpinski et al., 2003). The information on local geology was also considered when building the velocity model.

In this study, we test our method on several located microseismic events to invert for the complete moment tensor and estimate source parameters. The microseismic data from the bottom six geophones at a depth from 3912 m (12,835 ft) to 3944 m (12,940 ft) are selected due to their higher S/Ns. The P-waves on the upper six geophones are barely identifiable due to the greater distance from the events. The average S-wave S/N on the upper six geophones is also 10 dB lower than that on the bottom six geophones. Moreover, due to the poor clamping of vertical component geophones, the average S/N of the band-pass filtered vertical component data is at least 10 dB lower than that of the band-pass filtered horizontal component data. On the other hand, from Figure 3b, it is observed that two horizontal components have a similar capability in resolving the moment tensor as three components. Therefore, only the

**Figure 11.** The histograms of errors in the inverted source parameters (double-couple source). The source has a strike of 108°, a dip of 80°, and a rake of 43°. The source-receiver configuration is described in Figure 9. The rest of the figure description is analogous to Figure 10.



two horizontal components from the bottom six geophones are used in the following moment tensor inversion.

Figure 12 illustrates the horizontal plane view of the located events, with a monitoring well at the origin. The average fracture trend is seen along the N87°E or N-93°E direction (Sharma et al., 2004). Seven events at a depth from 3975 m to 3993 m are selected and plotted as red circles. The mean source-receiver distance for the selected events is around  $15\lambda_s$  (106.7 m). The average noise level as a percentage of maximum absolute signal amplitude is about 7% for the selected events, which is lower than the 10% noise level used in the synthetic study.

In the following section, we will begin with one event, named “test event 1,” to demonstrate the procedure of the constrained moment tensor inversion and source parameter estimation using full-waveforms. After that, we will present and discuss the results from all seven chosen events.

### Moment tensor inversion and source parameter estimation

As discussed in the synthetic study, for events that have a mean source-receiver distance greater than  $5\lambda_s$ , the complete moment tensor can be inverted from full-waveforms by imposing additional constraints. Warpinski and Du (2010) used direct P- and S-wave amplitudes from this one-well data set and applied a zero-trace (deviatoric source) constraint to invert for the source mechanisms and reported a large amount of scatter in the inverted strike and dip values.

In this study, instead of the deviatoric source constraint, a more realistic constraint on the fracture geometry is applied in the inversion. A conservative strike range of  $\pm 60^\circ$  around the average fracture trend and a dip range of  $60^\circ \sim 90^\circ$  is used as the type I constraint in this field example. The source parameters, including the fracture plane solution, seismic moment, and component percentages are estimated from the inverted complete moment tensor.

Figure 13 shows the constrained inversion for test event 1 with the type I constraint. The cyan strip gives the permissible range of  $m_{22}$  values. The  $m_{22}$  value is determined by the green vertical line representing the maximum DC percentage within the allowed strike and dip range. Thus, the complete moment tensor is obtained.

Figure 14a and b gives the waveform fitting for test event 1 between modeled and observed data. A good agreement of dominant P- and S-wave trains is seen in Figure 14a and b. This gives confidence in the event location and 1D velocity models. The unmodeled wave packages are probably due to random noise and unmodeled lateral heterogeneities.

The source parameters of test event 1 estimated from the complete moment tensor are listed in Table 4. The seismic moment for event 1 is around  $1.8 \times 10^4 \text{ N} \cdot \text{m}$ , suggesting a moment magnitude around  $-3.22$ . The two strike values estimated from the double-couple component correspond to the orientation of the fracture plane and the auxiliary plane, respectively. It is hard to distinguish the two planes with only one event. The estimated strike, dip, and rake values for all test events are listed in Table 4. The first set of values agrees well with the average fracture trend of N87°E or

N-93°E observed by Sharma et al. (2004) and is chosen as the fracture strike. Although the constraint used in the inversion assumes a strike range of  $\pm 60^\circ$  around the average fracture trend, the actual inverted strike values for the six out of seven events have a maximum deviation from the average fracture trend of less than  $\pm 35^\circ$ . In other words, additional information brought by the constrained inversion improves our a priori knowledge of source parameters, specifically the fracture strike. The difference between the inverted strike values and the average fracture trend comes from the fact that the orientation of small local fractures described by individual events differs from the average fracture orientation given by multiple event locations (Rutledge and Phillips, 2003). Noise contamination may also contribute to the difference.

Table 4 also summarizes the estimated component percentages. The results indicate a dominant double-couple component for most events. However, even considering the errors in the component percentage estimates as discussed in the synthetic study, a nonnegligible volumetric component is observed for some events, such as test events 3 and 6.

**Table 3. Statistics of double-couple microseismic source inversion with one-well data under different constraints (refer to Figure 11). Table caption is analogous to Table 2.**

Mean absolute errors in the inverted source parameters	Type of inversion constraints		
	I	II	III
Isotropic component percentage (%)	13	16	6
CLVD component percentage (%)	6	14	8
DC component percentage (%)	19	30	14
Seismic moment (%)	35	18	30
Strike ( $^\circ$ )	9	0	9
Dip ( $^\circ$ )	8	4	8
Rake ( $^\circ$ )	9	8	16

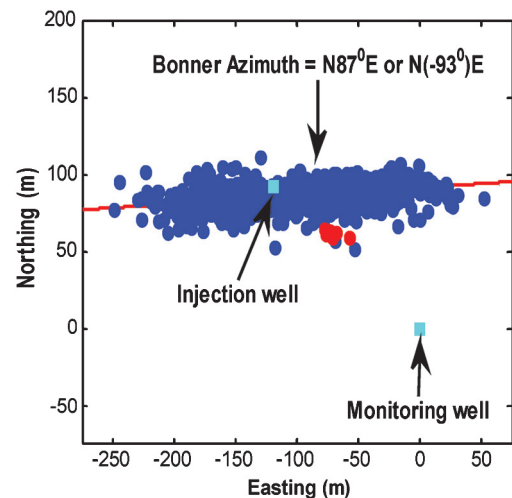


**Figure 12.** Horizontal plane view of microseismic event locations for the Bonner data set. Seven selected test events for moment tensor inversion are shown as red circles.

Figure 13. Constrained inversion for test event 1 with the type I constraint. The figure description is analogous to Figure 9.

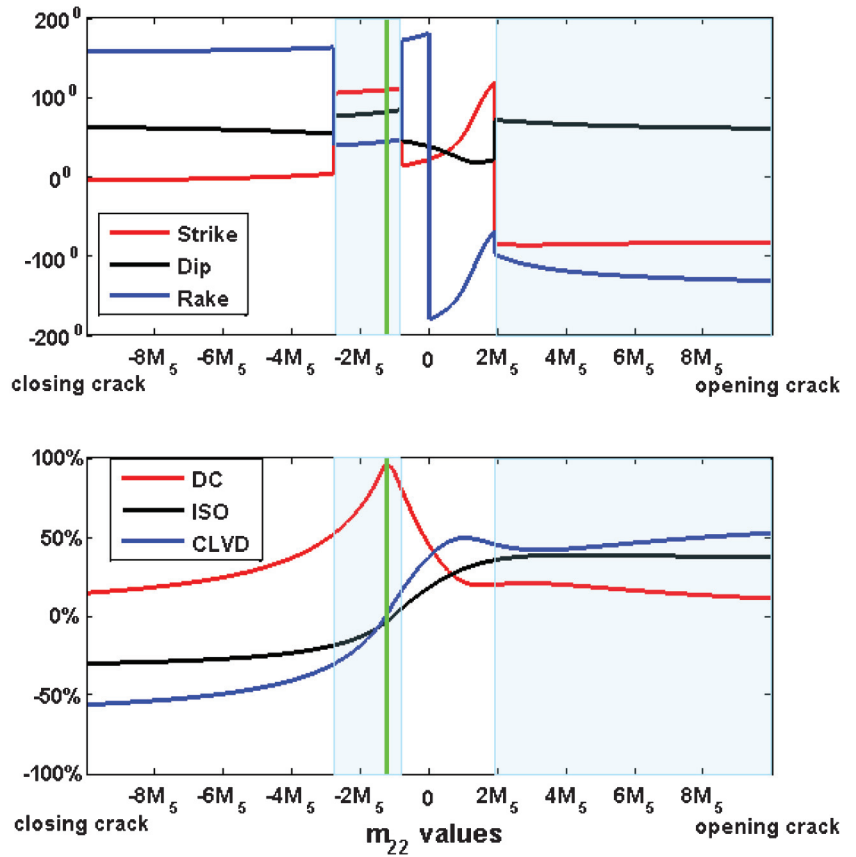
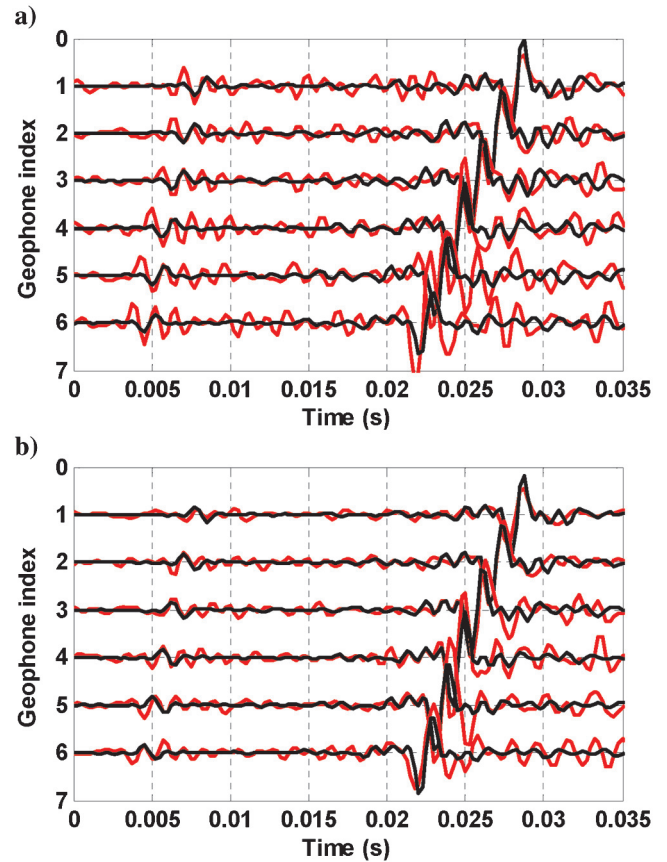


Figure 14. Waveform fitting for test event 1. Modeled seismograms derived from constrained inversion are shown in black, while the observed seismograms are plotted in red. (a) North component. (b) East component.





**Table 4. Results of source parameter determinations for the seven selected test events using constrained inversion with the type I constraint.**

Event	$M_0$	$M_W$	DC%	ISO%	CLVD%
	$10^4 \text{ N} \cdot \text{m}$		%	%	%
1	1.8	−3.22	96	1	−3
2	1.1	−3.66	68	3	−29
3	3.1	−3.06	52	48	0
4	5.8	−2.89	69	31	0
5	1.4	−3.30	87	−13	0
6	3.2	−3.05	45	55	0
7	3.3	−3.05	82	18	0

Event	Strike		Dip		Rake	
	Degrees		Degrees		Degrees	
1	108	10	81	47	43	167
2	107	14	62	83	8	152
3	−122	143	65	79	−168	−25
4	−128	−38	66	90	0	−156
5	−124	137	73	62	−151	−20
6	83	−17	63	71	−158	−29
7	138	−116	73	50	−43	−157

Note: The strike, dip, and rake values are defined according to the conventions set forth by [Aki & Richards \[2002\]](#).

For each event, the corner frequency is estimated from the far-field S-wave displacement spectrum ([Walter and Brune, 1993](#)). The approximate source radius is then determined from the corner frequency estimate according to [Madariaga's model \(Madariaga, 1976; Talebi and Boone, 1998\)](#). The corner frequencies of all seven test events range from 450 Hz to 750 Hz. The derived source radii indicate a small rupture area on the order of  $1 \text{ m}^2$ . The moment magnitude of the test events ranges from  $-4$  to  $-2$ , which is consistent with previous studies of hydrofracture events from down-hole observations ([Warpinski, 2009](#)).

## CONCLUSIONS

In this paper, we developed a full-waveform-based complete moment tensor inversion approach for hydraulic fracture monitoring using microseismic data recorded at a vertical borehole. The study involved both synthetic data and field data. The condition number study showed that two monitoring wells at an azimuthal separation of  $45^\circ$  have a similar resolving power of the moment tensor as eight wells with full azimuthal coverage. By exploring full wavefields in a layered medium instead of using only far-field direct P- and S-wave amplitudes, we demonstrated that the complete moment tensor can be retrieved for events that are close to the monitoring well. The near-field information and nondirect waves (i.e., reflected/refracted waves) propagated through a layered medium contribute to the decrease in the condition number. On the other hand, when

the events are in the far-field range, two monitoring wells are desirable for complete moment tensor inversion.

With synthetic tests, we demonstrated that the complete moment tensor from one-well data at far-field is possible if one imposes some constraints. Far-field tests with different constraints indicate that a priori information on fracture orientation helps recover the complete moment tensor and reduces the uncertainty of not only the fracture plane solution but also the seismic moment and moment component percentages. The synthetic study also shows that a reasonable amount of error in source location and the velocity model, together with random noise, does not cause a serious distortion in the inverted moment tensors and source parameters.

Proper constraints on the source play a big role in complete moment tensor retrieval using one-well data at far-field. The strike and dip range constraints were applied in a field study to invert for the complete moment tensor from one-well data at far-field. The results indicate the existence of both double-couple and nondouble-couple components in the source. The fracture strike values, derived by the inversion, generally agree with the average fracture trend determined from multiple event locations.

Potential errors in source parameter estimates from one-well data at far-field primarily come from the inaccuracies in the a priori information that has been used in the inversion. Future work will include testing the method against the results from two-well inversion. An extended study on the influence of velocity model errors will also be carried out in the future. The full-waveform approach has the potential to improve the source properties study of microseismic events monitored using borehole sensors even in a single well.

## ACKNOWLEDGMENTS

The authors would like to thank Pinnacle — A Halliburton Service for providing the data and for funding this research. We are grateful to Norm Warpinski, Jing Du, Erkan Ay, and Qinggang Ma from Halliburton Energy Services Company; Bill Rodi, H. Sadi Kuleli, and Michael Fehler from MIT for their helpful discussions. We thank Halliburton Energy Services Company and Anadarko Petroleum Corporation for permission to publish this work. We would like to thank the reviewers and the associate editors for the incisive and helpful comments. Their suggestions contributed significantly to the improvement of the paper.

## APPENDIX A

### RETRIEVAL OF $M_{22}$ FROM ONE-WELL DATA AT NEAR-FIELD

In this appendix, we study the ability to retrieve  $m_{22}$  using two horizontal component data from one vertical well at near-field. Previous studies have shown that, with far-field P- and S-wave amplitudes, it is impossible to invert for  $m_{22}$  using data from one vertical well ([Nolen-Hoeksema and Ruff, 2001; Vavryčuk, 2007](#)). In this study, we use a pure  $m_{22}$  source to generate synthetic seismograms. The true moment tensor, in this case, has only one nonzero element,  $m_{22} = 1$ . The source is comprised of 66.7% CLVD and 33.3% isotropic component. The source-receiver configuration is the same as the near-field study. We invert for the complete moment tensor with band-pass filtered horizontal component data after adding 10% Gaussian noise. During the inversion, we use the approximate velocity model and a spatial grid search around the

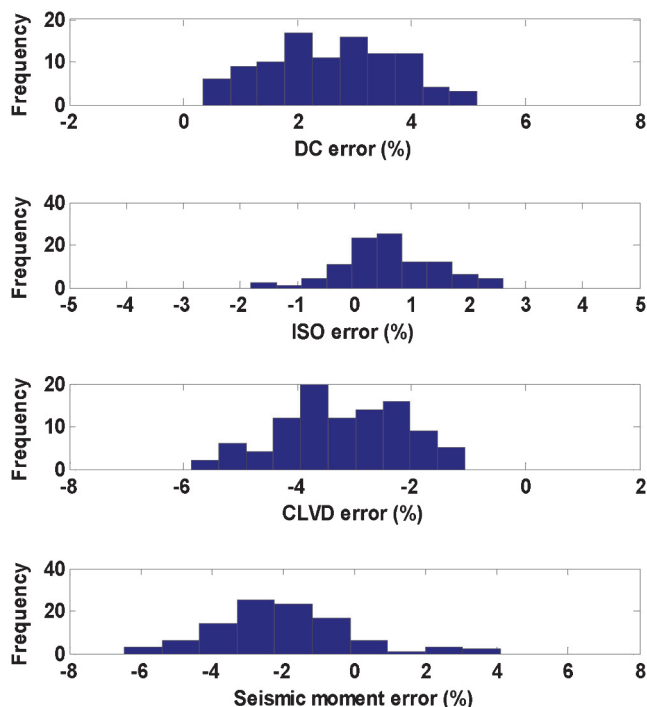


Figure A1. The histograms of errors in the inverted source parameters. The true moment tensor has only one nonzero element,  $m_{22} = 1$ . The source-receiver configuration is described in Figure 4, with an average source-receiver distance of 18.3 m (60 ft). The unconstrained inversion is performed with 10% Gaussian noise contaminated horizontal components from well B1.

mislocated source (see the main text for details). Figure A1 shows the source parameters derived from the inverted complete moment tensor. In this case, there is no double-couple component. Therefore, there is no definition for the strike, dip, and rake (Jechumtálová and Eisner 2008). The mean absolute errors in DC, ISO, and CLVD percentages are 3%, 1%, and 3%, respectively, while the mean absolute error in seismic moment is 2.4%. Considering the noise we add and the errors in the velocity model and source location we assume in the inversion, the errors in the inverted source parameters are negligible. This shows that complete moment tensor inversion can be inverted from near-field waveforms.

## REFERENCES

- Aki, K., and P. G. Richards, 2002, *Quantitative seismology* second edition: University Science Books.
- Baig, A., and T. Urbancic, 2010, Microseismic moment tensors: A path to understanding frac growth: *The Leading Edge*, **29**, 320–324, doi: [10.1190/1.3353729](https://doi.org/10.1190/1.3353729).
- Bouchon, M., 2003, A review of the discrete wavenumber method: *Pure and Applied Geophysics*, **160**, 445–465, doi: [10.1007/PL00012545](https://doi.org/10.1007/PL00012545).
- Eaton, D. W., 2009, Resolution of microseismic moment tensors: A synthetic modeling study: 79th Annual International Meeting, SEG, Expanded Abstracts, 3569–3573.
- Eisner, L., B. J. Hulse, P. Duncan, D. Jurick, H. Werner, and W. Keller, 2010, Comparison of surface and borehole locations of induced seismicity: *Geophysical Prospecting*, **58**, 809–820, doi: [10.1111/j.1365-2478.2010.00867.x](https://doi.org/10.1111/j.1365-2478.2010.00867.x).
- Griffin, L. G., R. B. Sullivan, S. L. Wolhart, C. K. Waltman, C. A. Wright, L. Weijers, and N. R. Warpinski, 2003, Hydraulic fracture mapping of the high-temperature, high-pressure Bossier sands in East Texas: *SPE Paper* 84489.
- Jechumtálová, Z., and L. Eisner, 2008, Seismic source mechanism inversion from a linear array of receivers reveals non-double-couple seismic events induced by hydraulic fracturing in sedimentary formation: *Tectonophysics*, **460**, 124–133, doi: [10.1016/j.tecto.2008.07.011](https://doi.org/10.1016/j.tecto.2008.07.011).
- Jost, M. L., and R. B. Herrmann, 1989, A student's guide to and review of moment tensors: *Seismological Research Letters*, **60**, 237–57.
- Madariaga, R., 1976, Dynamics of an expanding circular fault: *Bulletin of the Seismological Society of America*, **66**, 639–666.
- Nolen-Hoeksema, R. C., and L. J. Ruff, 2001, Moment tensor inversion of microseisms from the B-sand propped hydrofracture, M-site, Colorado: *Tectonophysics*, **336**, 163–181, doi: [10.1016/S0040-1951\(01\)00100-7](https://doi.org/10.1016/S0040-1951(01)00100-7).
- Pearson, C., 1981, The relationship between microseismicity and high pore pressures during hydraulic stimulation experiments in low permeability granitic rocks: *Journal of Geophysical Research*, **86**, 7855–7864, doi: [10.1029/JB086iB09p07855](https://doi.org/10.1029/JB086iB09p07855).
- Phillips, W. S., T. D. Fairbanks, J. T. Rutledge, and D. W. Anderson, 1998, Induced microearthquake patterns and oil-producing fracture systems in the Austin chalk: *Tectonophysics*, **289**, 153–169, doi: [10.1016/S0040-1951\(97\)00313-2](https://doi.org/10.1016/S0040-1951(97)00313-2).
- Phillips, W. S., J. T. Rutledge, and L. House, 2002, Induced microearthquake patterns in hydrocarbon and geothermal reservoirs: Six case studies: *Pure and Applied Geophysics*, **159**, 345–369, doi: [10.1007/PL00001256](https://doi.org/10.1007/PL00001256).
- Rutledge, J. T., and W. S. Phillips, 2003, Hydraulic stimulations of natural fracture as revealed by induced microearthquakes, Carthage Cotton Valley gas field, east Texas: *Geophysics*, **68**, 441–452, doi: [10.1190/1.1567212](https://doi.org/10.1190/1.1567212).
- Sharma, M. M., P. B. Gadde, R. Sullivan, R. Sigal, R. Fielder, D. Copeland, L. Griffin, and L. Weijers, 2004, Slick water and hybrid fracs in the Bossier: Some lessons learnt: *SPE Paper* 89876.
- Šílený, J., D. P. Hill, L. Eisner, and F. H. Cornet, 2009, Nondouble-couple mechanisms of microearthquakes induced by hydraulic fracturing: *Journal of Geophysical Research*, **114**, B08307, doi: [10.1029/2008JB005987](https://doi.org/10.1029/2008JB005987).
- Talebi, S., and T. J. Boone, 1998, Source parameters of injection-induced microseismicity: *Pure and Applied Geophysics*, **153**, 113–130, doi: [10.1007/s000240050187](https://doi.org/10.1007/s000240050187).
- Vavryčuk, V., 2001, Inversion for parameters of tensile earthquakes: *Journal of Geophysical Research*, **106**, 16339–16355, doi: [10.1029/2001JB000372](https://doi.org/10.1029/2001JB000372).
- Vavryčuk, V., 2007, On the retrieval of moment tensors from borehole data: *Geophysical Prospecting*, **55**, 381–391, doi: [10.1111/gpr.2007.55.issue-3](https://doi.org/10.1111/gpr.2007.55.issue-3).
- Walter, W. R., and J. N. Brune, 1993, Spectra of seismic radiation from a tensile crack: *Journal of Geophysical Research*, **98**, 4449–4459, doi: [10.1029/92JB02414](https://doi.org/10.1029/92JB02414).
- Warpinski, N. R., 1997, Microseismic and deformation imaging of hydraulic fracture growth and geometry in the c sand interval, GRI/DOE M-site project: *SPE Paper* 38573.
- Warpinski, N. R., 2009, Microseismic monitoring: Inside and out: *Journal of Petroleum Technology*, **61**, 80–85, doi: [10.2118/118537-MS](https://doi.org/10.2118/118537-MS).
- Warpinski, N. R., P. T. Branagan, S. L. Wolhart, and J. E. Uhl, 1998, Mapping hydraulic fracture growth and geometry using microseismic events detected by a wireline retrievable accelerometer array: *SPE Paper* 40014.
- Warpinski, N. R., and J. Du, 2010, Source mechanism studies on microseismicity induced by hydraulic fracturing: *SPE Paper* 135254.
- Warpinski, N. R., R. B. Sullivan, J. E. Uhl, C. K. Waltman, and S. R. Machovoe, 2003, Improved microseismic fracture mapping using perforation timing measurements for velocity calibration: *SPE Paper* 84488.